Lateral variations in compressional velocities beneath the Tibetan Plateau from P_n traveltime tomography

Lian-She Zhao[1] and Jiakang Xie[2]

[1]*Seismological Laboratory 252-21, California Institute of Technology, Pasadena, CA 91125, USA*
[2]*Department of Earth and Atmospheric Sciences, Saint Louis University, 3507 Laclede Avenue, St Louis, MO 63103, USA*

SUMMARY

A back-projection algorithm is applied to 353 P_n traveltime measurements to image the lateral variations in compressional velocity in the uppermost mantle in and around Tibet. Prior to the tomographic inversion, we refined the apparent P_n slowness measurements based on a recently developed relocation procedure (Zhao & Helmberger 1991), and mathematical formulations of Zhao (1993). These refinements are crucial in obtaining a high-quality velocity image.

We obtained an average P-velocity value for the uppermost mantle of $7.93\,\mathrm{km\,s^{-1}}$, and an average mantle P-velocity gradient of $3.1 \times 10^{-3}\,\mathrm{s^{-1}}$ for Tibet. The final 2-D P-velocity image in the uppermost mantle is characterized by a large ($7°$ to $9°$ in dimension) low-velocity (down to about $7.78\,\mathrm{km\,s^{-1}}$) region in north central Tibet, and by large high-velocity (up to $8.11\,\mathrm{km\,s^{-1}}$) regions in the western and eastern flanks of Tibet.

The crustal thickness is greater than $70\,\mathrm{km}$ inside the Tibetan plateau; it decreases toward the southern, eastern and western boundaries of the plateau. At and beyond these boundaries, the crustal thickness is similar to those beneath the Eurasian shield.

Rigorous analyses of resolution and error suggest that:

(1) there is a pronounced difference between the tomographic velocity image obtained with and without the refinements to the P_n-slowness measurements, indicating a significant improvement in the quality of our inversion by these refinements.

(2) Random errors in measuring earthquake origin times and locations, and in the P_n arrival times, should not cause errors of more than $0.1\,\mathrm{km\,s^{-1}}$ in the velocity image.

(3) The resolution is generally within $6°$ to $10°$.

The velocity image obtained in this study is consistent with previous S–P traveltime studies and geothermal/petrological studies, and is consistent with a mantle-convection model in which a convective upwelling is occurring in north central Tibet and downwellings occurring in the surrounding regions (Molnar 1988, 1990).

Key words: inversion, mantle, seismic tomography, Tibet.

INTRODUCTION

The Tibetan Plateau, the Himalaya and the Karakoram are the most spectacular consequences of the collision of the Indian subcontinent with the rest of Eurasia in Cainozoic time (Fig. 1). Accordingly, the deep structure beneath them provides constraints on both the tectonic history of the region and on the dynamic processes that created these structures (Molnar 1988).

There have been numerous studies of seismic-velocity structure beneath Tibet. Studies of surface waves (e.g. Boujot & Romanowicz 1992), P_{nl} waveforms (Holt &
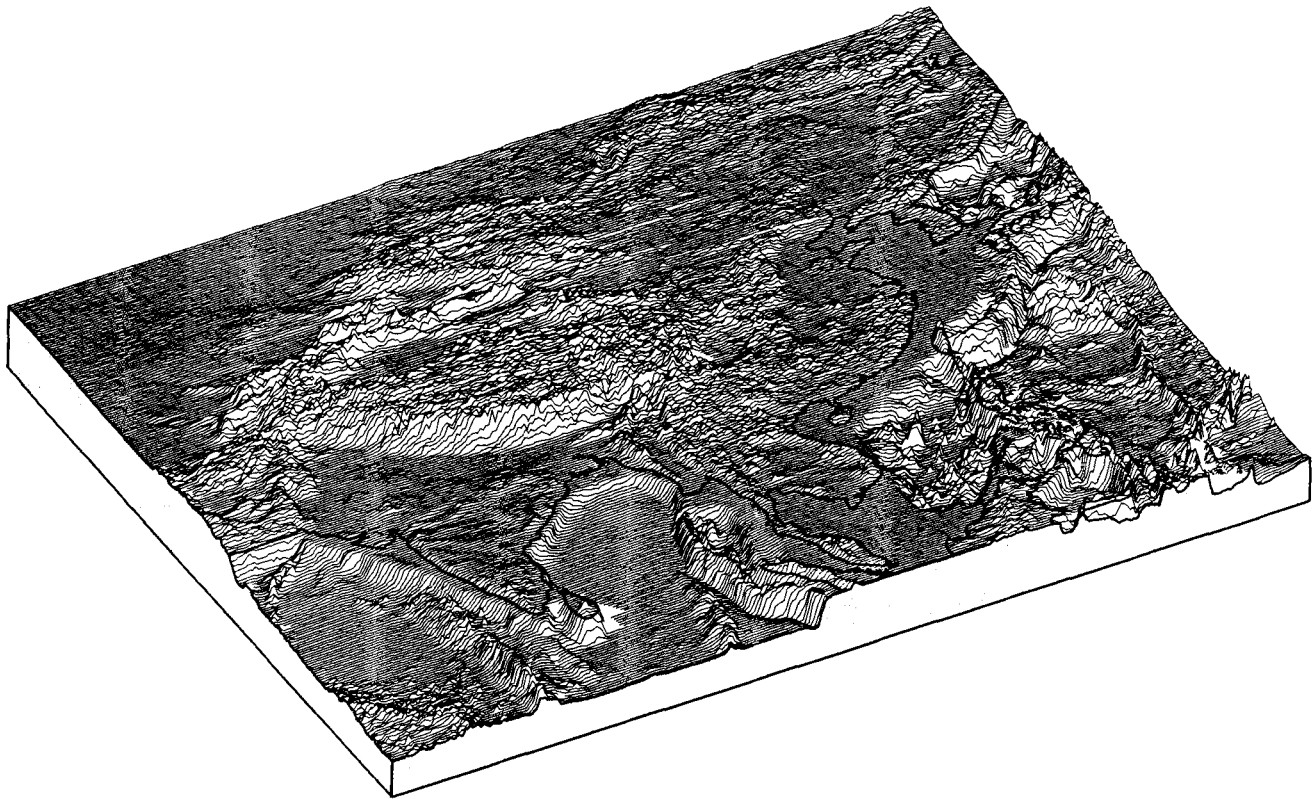
Figure 1. 3-D view of the topgraphy of the Tibetan Plateau and its surrounding regions.

Wallance 1990), and S–P differential traveltimes (Molnar & Chen 1984; Pettersen & Doornbos 1987; Molnar 1990) have indicated that there are significant lateral variations in seismic velocites in and around Tibet. There seemed to be a tendency for velocities to be lower in north central Tibet (Molnar 1990). This tendency, while inferred from very sparse data coverage, has been intriguing because of its suggestion of a probable convective upwelling in north central Tibet and downwellings in the surrounding region (Molnar 1988, 1990), which are in agreement with the observations of late Cainozoic volcanism in north central Tibet (Burge, Dewey & Kidd 1974; Deng 1978; Kidd 1975; Sengor & Kidd 1979; Molnar et al. 1987).

Previous tomographic inversions of P$_n$ traveltimes have been conducted in the western US (e.g. Hearn, Beghoul & Barazangi 1991). The P-wave velocity images from these inversions generally correlate well with the major tectonic features in those areas. In P$_n$ tomography, it is desirable to invert for the lateral variations of P-wave velocity in the uppermost mantle. When there is a velocity gradient in the upper mantle, however, P$_n$ observed at different distances samples mantle P-wave velocities through different depth ranges. This has been shown to be the case in Tibet (Song et al. 1985; Holt & Wallace 1990). Previous P$_n$ tomographies have ignored the effect of the mantle-velocity gradient. In an area where this gradient exists, images of lateral variations in P-wave velocity may be contamined by vertical variations in the mantle P-wave velocity. In this study, we apply the mathematical formulations of Zhao (1993), as well as the relocation procedure by Zhao & Helmberger (1991)

to 44 seismic events and 353 P$_n$ traveltimes to obtain P-wave slownesses along paths confined to the uppermost mantle. These slownesses are then input to a tomographic back-projection algorithm to obtain a laterally varying, 2-D P-wave velocity image in the uppermost mantle beneath the Tibetan Plateau.

DATA

We collected 353 P$_n$ arrival times from 44 earthquakes (Table 1) which occurred inside Tibet. Fig. 2 shows the ray coverage. The distance between source and receiver ranges between 3° to 15°. P$_n$ arrivals at greater distances were not used, because deep turning P waves arrive before P$_n$ beyond 18° (Zhao, Helmberger & Harkrider 1991). Among P$_n$ traveltimes, we repicked 42 to judge the reliability of the ISC reported arrivals. Generally, they agree within 0.5 s. We rejected the P$_n$ arrival times yielding apparent P$_n$ velocities that are less than 7 km s^{-1} or greater than 9 km s^{-1}.

The parameters of the events used in this study are obtained by the relocation procedure of Zhao & Helmberger (1991). These parameters are listed in Table 1. The number of the P$_n$-phase picks from each event is also listed in Table 1, under 'N'. Table 2 lists the station locations and vertical traveltime delays (b$_j$). The latter are calculated from the available regionalized models, including the models of Holt & Wallace (1990), Zhao et al. (1991), and Zhao & Helmberger (1993).

Table 1. Earthquakes used in this study.

Event	Date			Origin Time			Location		Depth	N‡
	Mo	Da	Yr	hr	min	sec	(°N)	(°E)	(km)	
1	3	16	64	1	5	13.5 ± 1.2	37.11	95.60	10	2
2	3	6	66	2	10	52.1 ± 0.8	31.50	80.53	11	4
3	3	6	66	2	15	49.8 ± 1.1	31.48	80.50	8	3
4	10	14	66	1	4	40.0 ± 1.2	36.50	87.46	8	7
5	8	15	67	9	21	-2.6 ± 0.9	31.23	93.56	8	2
6	8	30	67	4	22	01.8 ± 1.2	31.71	100.24	10	1
7	8	30	67	11	9	44.8 ± 1.4	31.73	100.28	8	1
8	3	24	71	13	54	15.2 ± 1.2	35.46	98.03	7	1
9	4	3	71	4	49	-2.2 ± 1.4	32.19	95.08	8	1
10	5	22	71	20	3	27.3 ± 1.3	32.42	92.11	8	3
11	8	30	72	15	14	05.0 ± 1.3	36.64	96.35	15	1
12	8	30	72	18	47	38.0 ± 1.2	36.71	96.46	19	2
13	2	6	73	10	37	06.1 ± 1.5	31.38	100.54	10	1
14	2	7	73	16	6	20.7 ± 1.3	31.58	100.28	8	1
15	7	14	73	4	51	16.1 ± 1.5	35.25	86.41	6	12
16	7	14	73	13	39	24.1 ± 0.7	35.30	86.51	7	10
17	11	18	77	5	20	06.7 ± 1.1	32.75	88.44	10	8
18	3	29	79	7	7	15.3 ± 1.3	32.55	97.28	10	7
19	2	22	80	3	2	42.8 ± 0.7	30.65	88.61	10	9
20	6	1	80	6	19	-5.2 ± 1.1	39.06	95.63	12	7
21	6	24	80	7	35	44.7 ± 1.2	33.02	88.46	11	10
22	7	29	80	14	58	39.4 ± 1.0	29.64	81.08	15	7
23	8	23	80	21	36	48.9 ± 1.5	33.07	75.69	14	6
24	8	23	80	21	50	-0.5 ± 2.0	32.89	75.83	13	6
25	10	7	80	9	32	03.0 ± 1.3	35.63	82.21	4	7
26	11	19	80	19	0	45.5 ± 0.9	27.47	88.80	14	8
27	1	23	81	21	13	46.5 ± 1.2	30.99	101.14	8	5
28	6	9	81	22	8	17.6 ± 1.3	34.65	91.34	10	9
29	1	23	82	17	37	25.8 ± 1.2	31.74	82.27	10	4
30	6	15	82	23	24	26.5 ± 1.2	31.91	99.92	7	11
31	2	13	83	1	40	08.2 ± 1.9	40.05	75.17	5	11
32	5	20	85	15	11	35.6 ± 0.5	35.62	87.28	8	20
33	6	20	86	17	12	43.5 ± 1.2	31.23	86.79	15	13
34	7	6	86	19	24	20.9 ± 1.2	34.55	80.15	5	22
35	8	20	86	21	23	51.2 ± 1.2	34.65	91.49	11	15
36	8	26	86	9	43	-1.2 ± 1.4	37.83	101.55	7	7
37	2	25	87	19	56	33.3 ± 0.8	38.12	91.13	15	15
38	12	22	87	0	16	38.5 ± 1.0	41.40	89.66	20	13
39	11	5	88	2	14	29.7 ± 1.1	34.34	91.79	8	21
40	4	15	89	20	34	06.9 ± 0.9	30.04	99.13	8	15
41	4	25	89	2	13	19.5 ± 0.9	30.05	99.43	8	14
42	5	3	89	5	53	-0.7 ± 0.9	30.07	99.49	9	12
43	5	3	89	15	41	30.0 ± 0.7	30.13	99.55	8	12
44	9	22	89	2	25	49.5 ± 1.0	31.61	102.52	12	7

† The event parameters are obtained by the relocation procedure of Zhao & Helmberger (1991). In particular, the latitudes and longitudes are determined using traveltimes, and the depths are determined by waveform modelling of *p*, *pP* and *sP* phases. For details, see Zhao & Helmberger (1991).

‡ N is the number of P_n arrivals available from the event.

INVERSE METHODS

In general, t_{ij}, the P_n traveltime from an *i*th source to a *j*th station can be expressed by

$$t_{ij} = V_{ij}^{-1} X_{ij} + a_i + b_j, \qquad (1)$$

where X_{ij} is the source-to-receiver horizontal distance, V_{ij} is the apparent *P*-wave velocity, a_i and b_j are vertical traveltime delays at the source and receiver, respectively (Hearn *et al.* 1991). Zhao (1993) shows that this relation is valid for the head waves travelling in complex waveguides, except that a_i and b_j should be calculated using local structures.

Method used to estimate a_i, b_j and mantle-velocity gradient

In previous studies, a_i and b_j are solved for iteratively. For this study, *a priori* knowledge of the averaged velocity structures within and outside Tibet is available (Holt & Wallace 1990; Zhao *et al.* 1991; Zhao & Helmberger 1993). Our approach is, therefore, to use this *a priori* knowledge to estimate a_i and b_j approximately, and subtract these approximate estimates from the traveltimes before the tomographic inversion.

Another difference between our method and previous inverse methods is that in the current inversion, we take into account the *P*-velocity gradient in the upper mantle, which is known to exist beneath the Tibetan Plateau (Song *et al.* 1985; Holt & Wallace 1990).

Numerically, both the approximate corrections for a_i, b_j and the corrections for mantle gradient are possible only with the recent formulations by Zhao (1993). These formulations relate the P_n traveltimes to the *P* velocities in the uppermost mantle in the presence of both lateral structural variations and a constant-velocity gradient in the upper mantle. To use these formulations, we rewrite eq. (1) as

$$\frac{1}{V_{ij}} = \frac{t_{ij} - a_i - b_j}{X_{ij}}. \qquad (2)$$

Denoting the estimates of a_i and b_j by a_i' and b_j', respectively, we have

$$\frac{1}{V_{ij}} \approx \frac{1}{V_{ij}'} = \frac{t_{ij} - a_i' - b_j'}{X_{ij}}. \qquad (3)$$

When a constant-velocity gradient is present, the mantle *P*-velocity distribution can be expressed as

$$V(z) = V(z_0)[1 + c(z - z_0)], \qquad (4)$$

where $V(z)$ is the depth-varying *P* velocity, z_0 is the depth of Moho, and *c* is a constant whose product with $V(z_0)$ gives the mantle-velocity gradient for a flat earth. For a spherical earth, the velocity gradient is $(c - 1.6 \times 10^{-4})V(z_0)$ when the units for *c* and $V(z_0)$ are km^{-1} and km s^{-1}, respectively (Helmberger 1973). Zhao (1993) shows that when such a constant-velocity gradient exists, V_{ij} in eqs (1) and (2) can be expressed as

$$V_{ij} = V_{ij}^0(1 + c^2 X_{ij}'^2/24), \qquad (5)$$

where V_{ij}^0 is the *P* velocity in the uppermost mantle averaged along the (*i*, *j*)th path, and X_{ij}' is the horizontal distance that a ray *travels in the mantle lid*. The derivation of eq. (5) is also given in the Appendix of this paper. Now we introduce a small residual

$$\epsilon_{ij} = [V_{ij}^0 - \bar{V}(z_0)][1 + c^2 X_{ij}'^2/24]$$
$$\approx V_{ij}^0 - \bar{V}(z_0) \quad \text{when} \quad c^2 X_{ij}^2 \ll 1, \qquad (6)$$

where $\bar{V}(z_0)$ is V_{ij}^0 averaged over all of the (*i*, *j*) pairs. Substituting eq. (6) into (5) leads to

$$V_{ij} = \bar{V}(z_0). \qquad (7)$$

In practice we must use V_{ij}' (eq. 3) instead of V_{ij} when eq. (7) is used; ϵ_{ij} will in that case contain, in addition to the right-hand side of eq. (6), contributions from non-zero δa_i
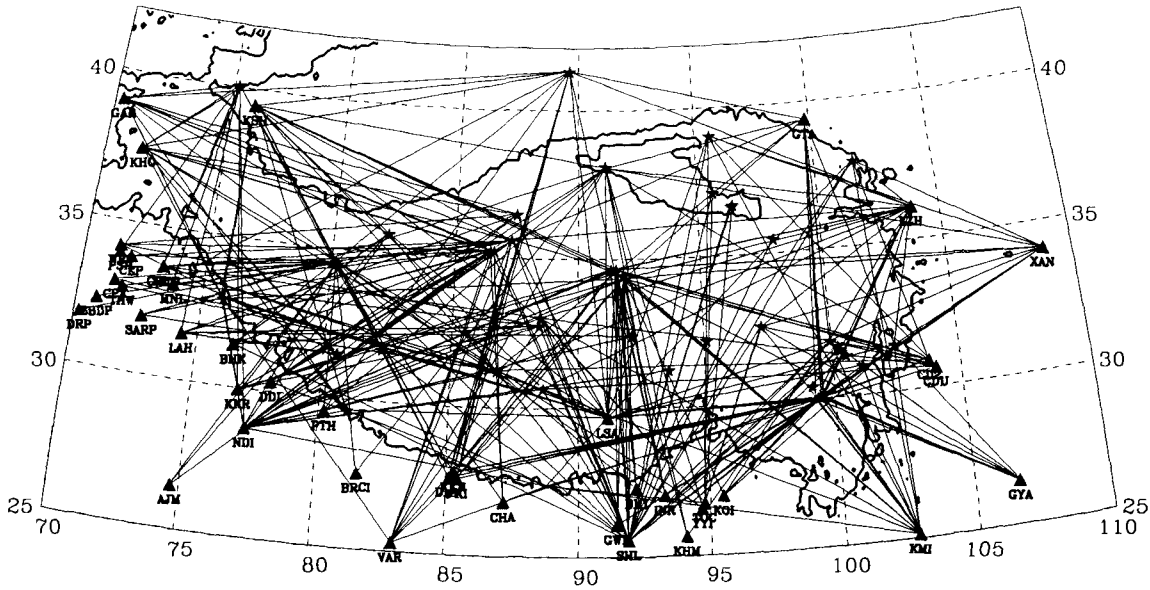
Figure 2. Ray paths. Triangles are stations. Stars are earthquakes. A heavy solid line is the contour of 3000 m altitude, which marks the boundary of the Tibetan Plateau.

and δb_j, defined as

$$\delta a_i = a_i' - a_i \tag{8}$$

and

$$\delta b_j = b_j' - b_j. \tag{9}$$

For an area where a number of different V_{ij}' are collected, $\bar{V}(z_0)$ and c can be solved by a linear regression using eq. (7).

Method used to obtain 2-D P velocities in the uppermost mantle

Once $\bar{V}(z_0)$ and c are solved, V_{ij}^0 can be estimated for each of the (i, j) pairs using eqs (3) and (5). Dividing the area under study into cells, we have from the definition of V_{ij}^0

$$\frac{1}{V_{ij}^0} = \frac{1}{X_{ij}'} \sum_k \Delta_{ijk} s_k + \mathrm{Res}_{ij}, \tag{10}$$

where Δ_{ijk} is the line segment over which the (i, j)th path overlaps the kth cell, s_k is the slowness in the kth cell, Res_{ij} is the slowness residual, which is caused by errors in event origin times/locations, in the traveltime readings, and in a_i' and b_j', which are approximations of a_i and b_j and are used to calculate V_{ij}^{-1} (eq. 3). Strictly speaking, deviations of the real uppermost mantle from a gridded, smoothly varying surface will also contribute to ϵ_{ij}; effects of this kind are known as the 'modelization errors' (e.g. Tarantola 1987). Eq. (10) forms a standard-linear-inverse problem for unknown s_k. We use a variation of the back-projection, or SIRT algorithm (e.g. Humphreys & Clayton 1988), described in detail by Xie & Mitchell (1990) to solve for s_k.

Method used to estimate crustal thicknesses

In the back-projection calculation, s_k values are updated during the iterations to reduce the misfit between the

inverse of V_{ij}^0 and $(1/X_{ij}') \sum_k \Delta_{ijk} s_k$. When the misfit stops decreasing, we end up with the final slowness model (final values of s_k) and some non-dimenished Res_{ij} values. To the first-order approximation we assume that Res_{ij} values are dominately caused by a_i' and b_j', the imprecise estimates on a_i and b_j prior to the back-projection inversion, we then have

$$\mathrm{Res}_{ij} \approx \frac{\delta a_i + \delta b_j}{X_{ij}}. \tag{11}$$

At the time we obtain Res_{ij}, a_i' and b_j' are known, and a_i and b_j (therefore, δa_i and δb_j) are not. Non-zero δa_i and δb_j values primarily result from the lack of smaller scale variations in the crustal structure used to calculate a_i' and b_j' prior to the inversion. With the known Res_{ij} values, we can solve for δa_i and δb_j to obtain a_i and b_j values, which can then be used to infer the smaller scale crustal thicknesses (this is just a calculation inverse to that with which we obtained a_i' and b_j'). To make the inversion for δa_i and δb_j overdetermined, and to reduce the probable effects of errors in origin times (Table 1), in event locations (Zhao & Helmberger 1991) and in P_n arrival-time readings (which also contribute to Res_{ij}), we merge the unknowns δa_i and δb_j into a new set of unknowns. To do so we divide the area under study into subregions with the following properties: (1) each of the lth subregion contains either a group of sources or a group of stations, called a 'subregion of sources' or a 'subregion of receivers'; (2) within each subregion, all of the a_i' and b_j' calculated for locations inside it have been constant, and (3) the geographic extent of each of the lth subregion is small, so that the crustal thickness of each subregion can be assumed constant. We now assume that δa_i and δb_j are constants within a given subregion, i.e.

$$\delta a_i = \tau_l \tag{12}$$

for all of the ith sources located within the lth subregion of

Table 2. Stations used in this study.

Name	Location ($^\circ$N)	Location ($^\circ$E)	b'_j † (sec)	N ‡
AJM	26.467	74.650	4.3	3
BRCI	27.567	81.580	3.6	2
BMI	27.300	92.200	3.6	3
BHK	31.417	76.417	4.3	4
CD2	30.910	103.758	5.1	10
CDU	30.660	104.011	5.1	6
CEP	33.824	71.909	4.3	2
CHA	26.833	87.167	3.6	4
CHCP	33.658	73.260	4.3	3
CPA	32.980	71.424	4.3	2
DDI	30.317	78.051	4.3	5
DMN	27.609	85.106	3.6	10
DRP	31.744	70.203	4.3	1
GAR	39.000	70.317	6.5	11
GTA	39.400	99.800	6.0	11
GWH	26.100	91.467	3.6	5
GYA	26.459	106.664	3.5	9
INR	27.050	93.283	4.4	7
JHI	26.733	94.167	5.1	4
JMU	32.717	74.900	3.6	2
KHM	25.651	94.068	5.1	3
KHO	37.483	71.533	6.5	13
KKN	27.784	85.268	3.6	10
KKR	29.951	76.817	4.3	6
KMI	25.123	102.740	4.1	16
KOI	26.983	95.500	5.1	5
KSH	39.450	75.968	6.0	15
LAH	31.550	74.333	4.3	8
LSA	29.700	91.150	6.9	24
LZH	36.084	103.834	6.0	19
MNL	33.135	73.750	4.3	3
NDI	28.683	77.217	4.3	24
NIL	33.650	73.250	4.3	6
PKI	27.571	85.409	3.6	9
PSH	33.937	71.434	4.3	1
PTH	29.550	80.217	5.2	4
SARP	31.922	72.670	4.3	3
SBDP	32.300	70.800	4.3	1
SHL	25.567	91.883	3.6	36
SRNI	33.950	74.750	4.3	1
THW	32.794	71.743	4.3	3
TOC	26.750	94.767	5.1	5
VAR	25.300	83.017	3.6	14
WRS	34.150	71.401	4.3	5
XAN	34.034	108.917	3.6	13
YYI	26.567	94.683	5.1	2

† b'_j is vertical traveltime from Moho to station.
‡ N is number of P_n traveltimes used to calculate b'_j.

sources, or

$$\delta b_j = \tau_l \tag{13}$$

for all of the jth station located within the lth subregion of stations. τ_l thus introduced form a new set of variables which is smaller in size than the unknowns δa_i and δb_j, provided that the number of subregions is small. Using Res_{ij}, we can now solve for τ_l in an overdetermined least-squares problem.

AVERAGE P_n VELOCITY AND MANTLE VELOCITY GRADIENT

The a'_i values are obtained with a laterally homogeneous velocity model (model TIP of Zhao *et al.* 1991). Values of b'_j are calculated from the models of Holt & Wallace (1990) and of Zhao *et al.* (1991). The resulting b'_j values are listed in Table 2.

The a'_i and b'_j values thus obtained are then subtracted from t_{ij} values to obtain apparent P_n-velocity values, which were subsequently multipled by a factor of $(R_E - D)/R_E$ to correct for a first-order effect of the earth's sphericity, where R_E (=6371 km) and D (=55 km) are defined as the average radius of the earth and the average crustal thickness in the area under study, respectively. The resulting apparent P_n-velocity (V'_{ij} in eq. 3) values are plotted in Fig. 3 against distance (X'_{ij}). In Fig. 3, the trend of increasing V'_{ij} with X'_{ij} is obvious, indicating the existence of the mantle-lid P-velocity gradient. We used the method described in the last section to invert for $\bar{V}(z_0)$ and c, (eq. 7). The results are

$$\bar{V}(z_0) = 7.93 \pm 0.17 \text{ km s}^{-1}, \tag{14}$$

and

$$c = 5.5 \times 10^{-4} \text{ km}^{-1}. \tag{15}$$

For X'_{ij} less than about 1700 km, it is clear that the condition in eq. (6) is valid. The $\bar{V}(z_0)$ and c values thus estimated predict the solid line in Fig. 3, with the dashed lines representing the standard deviations. Eq. (14) gives, for the uppermost mantle in Tibet, an averaged P velocity that agrees well with 7.94 km s^{-1} by Song *et al.* (1985). This value is, on the other hand, lower than 8.11 km s^{-1} by Jia & Chao (1981) and 8.12 km s^{-1} by Chen & Molnar (1981). The difference may be caused by the relocation and correction of mantle-velocity gradient, both are conducted in this study. Our value of 7.93 km s^{-1} is also lower than 8.24 km s^{-1} by Holt & Wallace (1990), and 8.29 km s^{-1} by Zhao *et al.* (1991), both were obtained by using long-period body waveforms which sample deeper parts of the mantle.

Equations (14) and (15) mean that the average velocity gradient in the lithosphere beneath the Tibetan Plateau and its surrounding regions is about $3.1 \times 10^{-3} \text{ s}^{-1}$ for the upper 150 km of mantle, after correcting the effect of the earth's sphericity. Song *et al.* (1985) obtained a depth-dependent velocity model for the upper mantle in Tibet. We have applied a least-squares fitting to their velocity values in the upper 150 km of mantle and obtained a velocity gradient of $2.9 \times 10^{-3} \text{ s}^{-1}$, which agrees well with our estimate. Holt & Wallace (1990) obtained a rough estimate of $2.5 \times 10^{-3} \text{ s}^{-1}$ for the same velocity gradient, a value not significantly different from our estimate.
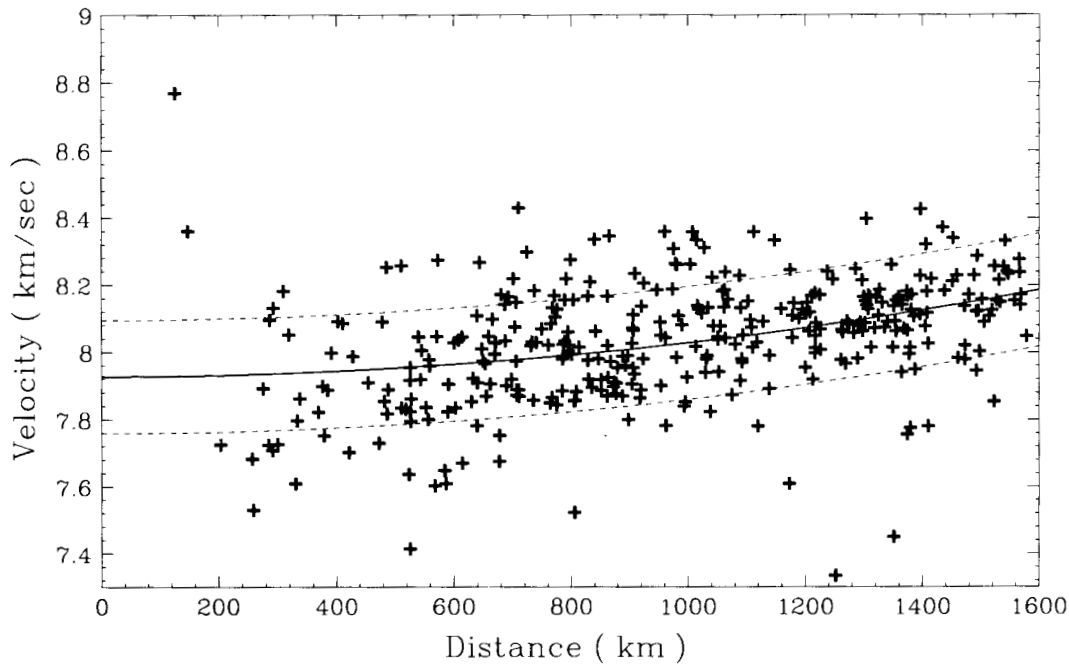
Figure 3. P_n traveltime data used in this study. The abscissa is distance travelled by the head wave in the mantle. A tendency for the traveltimes to be dependent on the distances can be easily seen. The solid line represents the linear regression fitting of eq. (5), corresponding to an average P velocity in the uppermost mantle of $7.93\ \mathrm{km\ s^{-1}}$ and an average of mantle P-velocity gradient of $4.4 \times 10^{-3}\ \mathrm{s^{-1}}$ (including the Earth's sphericity). Dashed lines represent the standard errors of the fitting.

LATERAL VARIATIONS IN P_n VELOCITIES AND CRUSTAL THICKNESS

The constant c in eq. (15) and a_i', b_j' terms obtained were used to estimate V_{ij}^0 values (eq. 5), which were then used in the back-projection tomography to solve for slowness, s_k (eq. 10). We divided the area in and around Tibet covered by the ray paths in Fig. 2 into 984 cells of a size of 1.5° by 1.5°. Convergence in the back-projection calculation takes place after 20 iterations. The resulting 2-D P-velocity image is shown in Fig. 4.

To estimate the lateral variations in the crustal thickness using the inverse method described earlier, we divided the area under study into 28 subregions. We set a linear
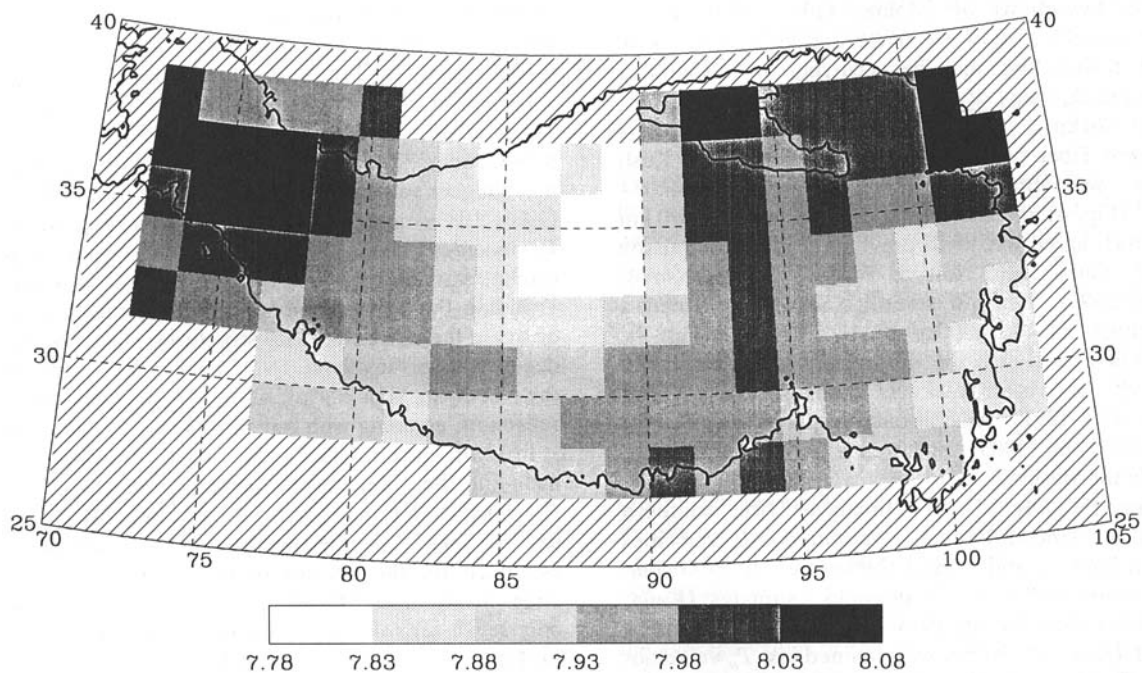
Figure 4. 2-D P-velocity image for the uppermost mantle underneath the Tibetan Plateau.
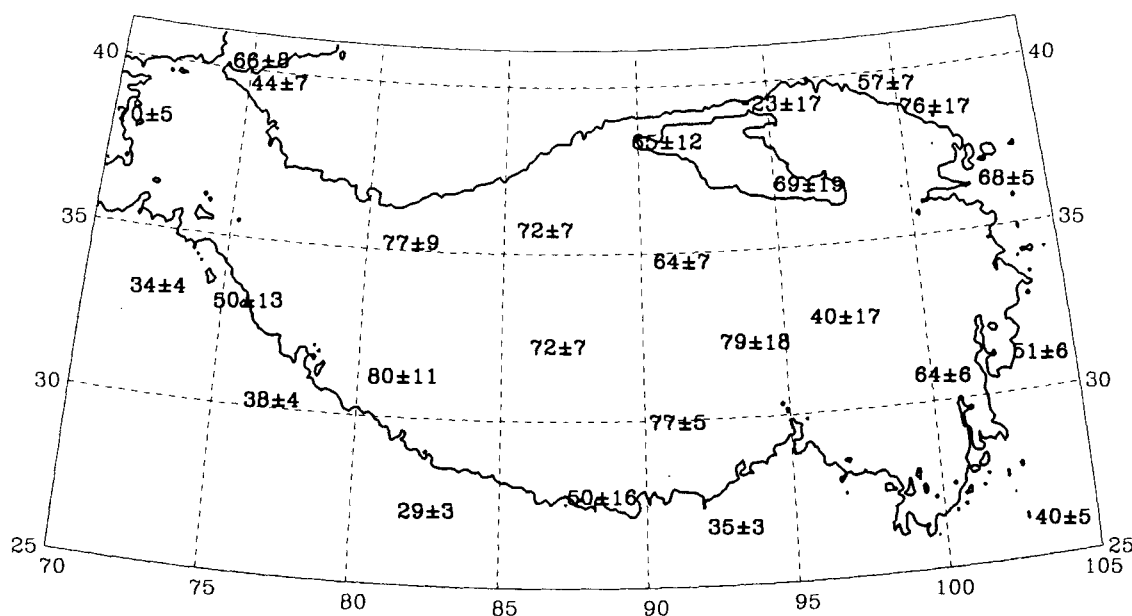
Figure 5. Crustal thicknesses of subregions (Table 3).

least-squares problem to solve for τ_i, which are then used to estimate crustal thicknesses within the subregions (Table 3 and Fig. 5).

The overall pattern of the 2-D P-velocity image in Fig. 4 is characterized by a low-velocity (down to about 7.78–7.83 km s^{-1}) region in north central Tibet, and high-velocity regions in the north-eastern and western flanks of Tibet. This correlates well with the regional variations in S–P traveltimes reported by Molnar & Chen (1984), Pettersen & Doornbos (1987) and Molnar (1990), and with the locations where young, late Cainozoic volcanic rocks have been observed (Burke *et al.* 1974; Kidd 1975; Deng 1978; Sengor & Kidd 1979; Molnar *et al.* 1987). These support the hypothesis by Molnar (1988, 1990) that a convective upwelling may be occurring in north central Tibet, and downwelling may be occurring in surrounding regions. In Fig. 5, many of the areas inside Tibet have very thick crust (>70 km).

For western Tibet (west to 80°E), including Hindu Kush and Pamir, we obtained P-wave velocities of 8.03–8.11 km s^{-1} (Fig. 4) and the crustal thicknesses of 65–70 km (Fig. 5), which agree well with previous studies (Beloussov *et al.* 1980; Kaila 1981; Holt & Wallace 1990; Zhao & Helmberger 1993). Beneath station KSH we obtained a crustal thickness of 44 km (Group 11 of Table 3; Fig. 5). This station is located near the western margin of the Tarim Basin, where the crustal thickness changes rapidly (Feng 1985; Zhao *et al.* 1991). This probably explains why Feng *et al.* (1981) and Feng (1985) suggested a crustal thickness of 50 km inside the Basin.

Along the foothills of the Himalayas (the southern boundary of the Tibetan Plateau), we obtained P_n velocities of 7.85–8.01 km s^{-1}, and crustal thicknesses of 29–38 km. These are consistent with the previous estimates (Kaila, Reddy & Narin 1968; Verma 1974; Holt & Wallace 1990).

In central Tibet (80°–90°E), we obtained low P_n velocities of 7.79 to 7.95 km s^{-1}. Holt & Wallace (1990, Fig. 9b) suggested a much higher velocity of 8.24 km s^{-1}, which may

result from the effect of velocity gradient in the mantle. Our estimated crustal thicknesses range between 72 and 80 km. consistent with 71.9 km by Holt & Wallace (1990).

In the Lhasa block, there have been three Sino–Franco DSS profiles: profile 1 runs between (28.8°N, 85.5°E) and (28.6°N, 90.3°E). Profiles 2 and 3 run between (32.3°N, 91.4°E) and (27.4°N, 89.2°E), and between (32.0°N, 89.1°E) and (32.0°N, 94.5°E), respectively. For this block, we obtained P_n velocities of 7.88 to 8.00 km s^{-1}, and crustal thicknesses of 75 km in the north, and 50 km in the south. The crustal thickness from interpreting the DSS profiles were 70–77 km along profile 1 (e.g. Hirn *et al.* 1984a; Teng *et al.* 1983b; Teng, Yin & Xiong 1985b; Xiong, Teng & Yin 1985); 75 to 40 km from north to south along profile 2 (e.g. Hirn *et al.* 1984b, 1984c; Hirn & Sapin 1984; Institute of Geophysics 1981; Teng *et al.* 1983a); and 70 km along profile 3 (Sapon *et al.* 1985; Teng *et al.* 1985b). Along profile 1, Teng *et al.* (1983b, 1985a) suggested P_n velocities of 8.1–8.2 km s^{-1}, whereas Hirn *et al.* (1984a) suggested a much higher value of 8.7 km s^{-1}. Along profile 2, Teng *et al.* (1981; 1983a) and Institute of Geophysics (1981) estimates P_n velocities to be 7.95–8.4 km s^{-1}. These wide ranges in the estimates of P_n velocities may be caused by many factors, including the ambiguity of P_n arrivals, the dipping Moho, errors in the crustal-velocity structures used, and the narrow distance ranges involved. INDEPTH reflection profile across the Tethyan Himalaya also showed a 75 km Moho reflection, agreeing with our results (Nelson *et al.* 1993).

In south-eastern Tibet (south to 35°N and east to 95°E), including the Yunnan and Sichuan provinces, we obtained P_n velocities that increase from 7.81 km s^{-1} in the south-east to 7.95 km s^{-1} in the north-west. The crustal thickness estimated for the interior of this area is subject to fairly large uncertainties (40 ± 17 km; see Fig. 5). This is because only seven arrivals are available for the estimate (group 21 in Table 3). The real averaged crustal thickness near that location may well be above 60 km. Our estimated crustal thickness is 40 ± 5 km beneath station KMI and 51 ± 6 km

Table 3. Vertical traveltime corrections for subregions (τ_l).

Sub-region	Stations or Events	τ_l	N†
1	GAR,KHO	0.78±0.52	24
2	CPA,CEP,CHCP,DRP,JMU-0.84±0.41		41
	LAH,MNL,NIL,PSH,SBDP		
	SRNI,SARP,THW,WRS		
3	AJM,BHK,DDI,KKR,NDI	-0.41±0.37	46
	PTH		
4	BRCI,CHA,KKN,KMN,PKI-0.70±0.35		49
	VAR		
5	BMI,GWH,INT,JHI,KHM	-0.13±0.30	70
	KOI,SHL,TOC,YYI		
6	GYA,KMI	-0.06±0.50	25
7	CD2,CDU	0.02±0.59	16
8	XAN	-0.36±0.66	13
9	LZH	0.80±0.54	19
10	GTA	-0.28±0.71	11
11	KSH	-1.42±0.61	15
12	ev25,ev34	0.77±0.45	29
13	ev2,ev3,ev22,ev29	0.88±0.57	18
14	ev26	-0.69±0.82	8
15	ev4,ev15,ev16,ev32	0.47±0.37	49
16	ev17,ev19,ev21,ev33	0.49±0.38	40
17	ev31	0.18±0.72	11
18	ev37	0.06±0.60	15
19	ev29,ev35,ev39	0.08±0.36	45
20	ev5,ev9,ev10	0.85±0.95	6
21	ev18	-1.17±0.89	7
22	ev6,ev7,ev13,ev14,ev27	0.08±0.30	80
	ev30,ev40,ev41,ev42		
	ev43,ev44		
23	ev1,ev8,ev11,ev12	0.28±0.98	6
24	ev20	-4.49±0.88	7
25	LSA	0.65±0.48	24
26	ev23,ev24	-0.68±0.70	12
27	ev36	0.65±0.88	7
28	ev38	0.30±0.65	13

† N is number of traveltime residuals ($\delta a'_i$ or $\delta b f'_j$) used to estimate τ_l.

beneath stations CDN/CD2 (Fig. 5). These results agree with, within the uncertainties, the P_n velocities and crustal thicknesses determined by Holt & Wallace (1990). Other studies have suggested a changing crustal thickness from 37 to 70 km, and a changing P_n velocity from 7.75 to 8.10 km s^{-1} (e.g. Feng 1985; Hu et al. 1986; Zhu et al. 1986; Ziong et al. 1986; Zhao & Zhang 1987; Yin et al. 1988; Kan & Lin 1988).

ANALYSIS OF RESOLUTION AND ERROR

Resolution of the P-velocity image

In computerized tomography, the spatial resolution at a given cell can be approximated by the point-spreading function (PSF) calculated for the cell (e.g. Humphreys & Clayton 1988; Xie & Mitchell 1990). Figs 6(a), (b) and (c) show PSF at three representative cells located in western,

central and eastern Tibet, respectively. As illustrated by these examples, the spreading of the PSF (and, therefore, the resolution) is generally within about 10°. At some locations where the ray coverages are relatively denser, the spreadings become less than 6° (Fig. 6b).

Effects of random errors on P-velocity image

The random errors in event locations and origin times, and in the P_n traveltime readings can cause random errors in the 2-D P-velocity image. The events used in this study have been relocated, the errors in origin times are given in Table 1. Since there is a direct relationship between the errors in event-origin times and the errors in event locations, the errors listed in Table 1 actually represent combined errors in all of the event parameters, including both event origin times and event locations (Zhao & Helmberger 1991). There are also probable errors in the ISC picks of the P_n arrival times, for which we estimated a maximum deviation of 1 s. The estimated maximum amplitude of the probable errors in our own picks is 0.5 s. We think these are good estimates since the events are fairly large ($m_b > 5.5$). To estimate the random errors in the P-velocity image caused by these errors and uncertainties, we used the estimated amplitudes for the latter and a pseudo-random sign generator (Xie & Mitchell 1990) to generate synthetic errors in traveltime measurements. For details and advantages of using this random error generator, the reader is referred to Xie & Mitchell (1990).

Figure 7 shows the resulting estimates of the random errors. For areas inside Tibet, the estimated random errors are less than about 0.02 km s^{-1}. The errors increase toward the boundaries of Tibet because of poorer ray coverages, but the values of errors there are still quite small (less than 0.05 km s^{-1}), with two expectionally larger values in the north-west and south-west corner. We note, however, that the estimated random errors might be smaller than the 'modelization errors' including those metnioned before, and those caused by anisotropy.

Sensitivity of 2-D P-velocity image to mantle-velocity gradient

To see how sensitive the 2-D P-velocity image in Fig. 4 is to the correction of mantle-velocity gradient, we conducted back-projection inversion using apparent P_n velocities (V'_{ij} in eq. 3) without correcting for that gradient, i.e. we replaced V^0_{ij} in eq. (10) by V'_{ij} in the sensitivity test. The resulting P-velocity image is plotted in Fig. 8. In this figure, the main features of the lateral variations in P-velocity image is roughly the same as that from inversion with the correction for the gradient (Fig. 4). However, the average velocity in Fig. 8 is higher (8.04 ± 0.18 km s^{-1}). This velocity is close to those obtained by Jia & Chao (1981) and by Chen & Molnar (1981), but lower than those by Holt & Wallace (1990) and by Zhao et al (1991), who used long-period waves. From Figs 4 and 8, corrections of the mantle-velocity gradient do not greatly affect the patterns of lateral variations in the tomographic images of P_n velocity, but affect significantly the average values of the images.

The velocity gradient in the upper mantle may have lateral variations, which can not be resolved using the
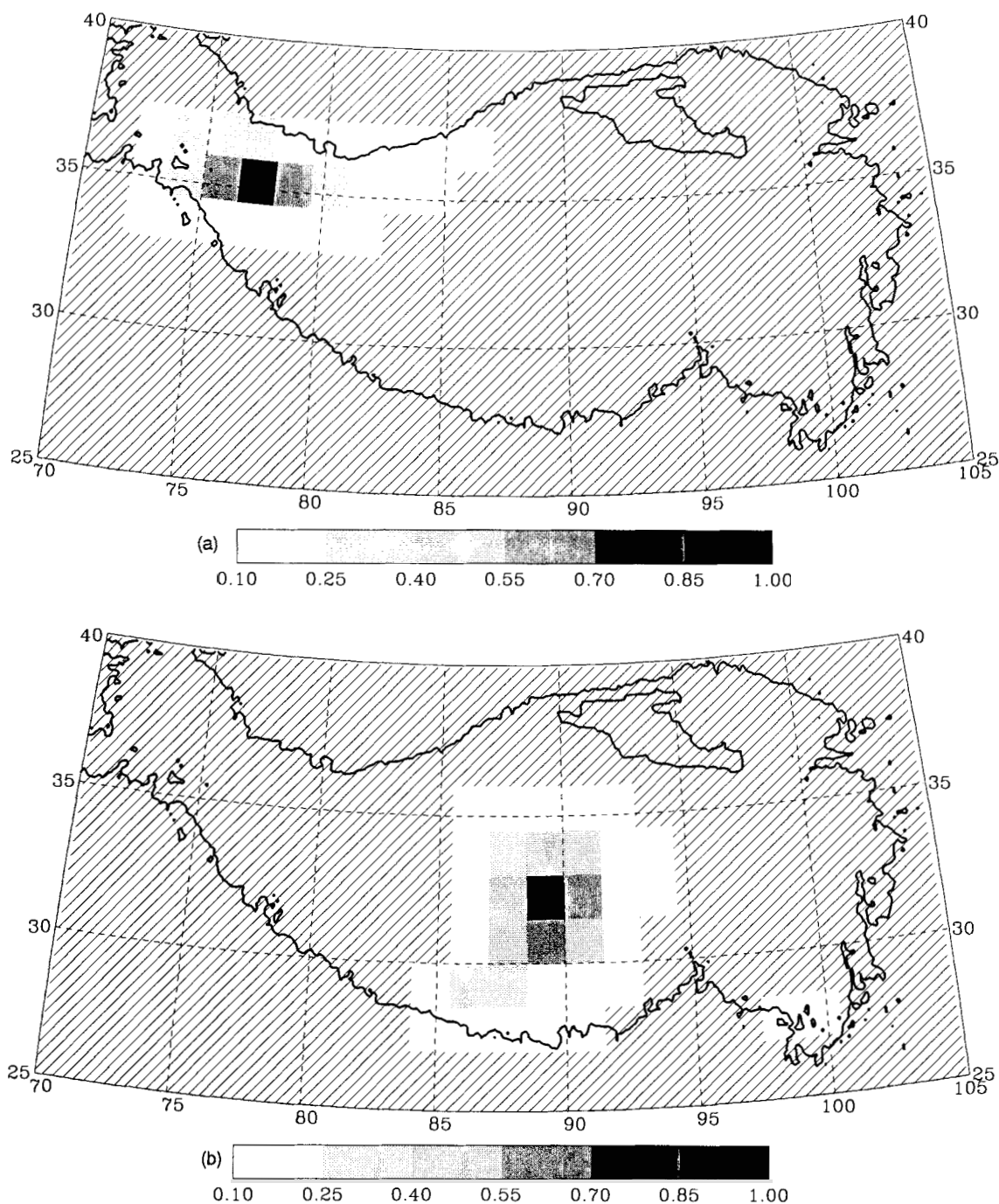
Figure 6. Point-spread functions (PSF). (a) PSF at a location in the Karakoram region of western Tibet, the PSF spreads out to 8°; (b) near the centre of Tibet, about 6°; (c) at a location in eastern Tibet, about 8°.

current data set. Based on *P*-wave traveltime tomography for volcanic regions, Zhao, Hasegawa & Hirouchi (1992) suggested that an upwelling may have a velocity gradient that is higher by about $1.0 \times 10^{-3}\,\text{s}^{-1}$ than in the surrounding regions. If this is true for north central Tibet, the P_n velocities there would be even lower than in Fig. 4.

Effects of vertical traveltimes at sources and receivers

To see the effect of the a_i' and b_j' values on the final P_n velocity image, we conducted an inversion in which we estimated a_i' and b_j' using model TIP only, corresponding to a constant value of 6.9 s for vertical traveltimes from surface to Moho. The mantle-velocity gradient is not corrected in this testing inversion, which results in the *P*-velocity image plotted in Fig. 9.

The average velocity of $8.19 \pm 0.17\,\text{km s}^{-1}$ in Fig. 9 is even higher than that in Fig. 8. The main feature of a slower velocity region in northern central Tibet in Figs 4 and 8 seem to be preserved in Fig. 9, but the velocities near the boundary of Tibet in Fig. 9 becomes faster. This is particularly pronounced for cells near the western end and
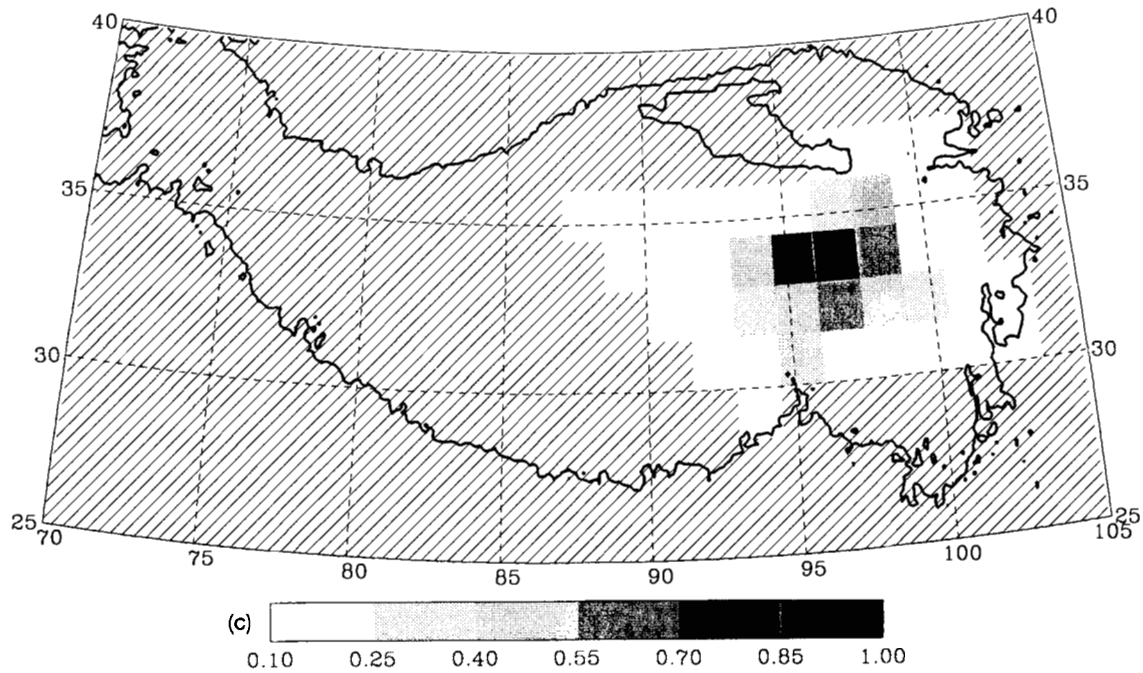
Figure 6. (*Continued.*)

the middle of the southern boundary. This phenomenon can be explained by a thinner crust near the boundaries of Tibet, where the crustal thicknesses can be as small as 30 to 35 km. Model TIP predicted a universal 70 km thick crust, which is most inadequate near the boundaries, and leads to overestimated mantle velocities there. Nevertheless, the effects of ignoring the mantle-velocity gradient and the lateral variations in vertical station-to-Moho traveltimes

have not significantly altered the main pattern of lateral variations in P-velocity image, and the average value of the P-velocity image seems to be affected much more.

Effect of event relocation on P-velocity image

Previous P_n studies used event parameters and P_n arrival times directly from the ISC bulletins. This has been the case
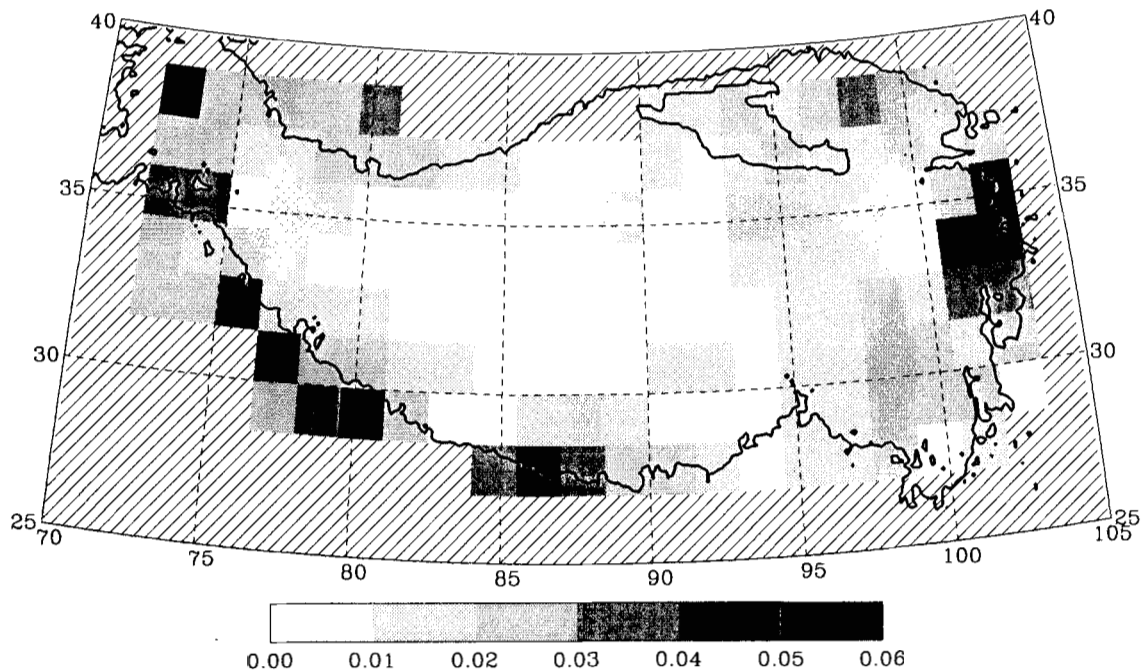
Figure 7. Map of the estimated random errors in the 2-D P-velocity image. Inside Tibet, the error is less than $0.02 \, \mathrm{km \, s^{-1}}$. The error on the Tibetan boundary is generally less than $0.05 \, \mathrm{km \, s^{-1}}$.
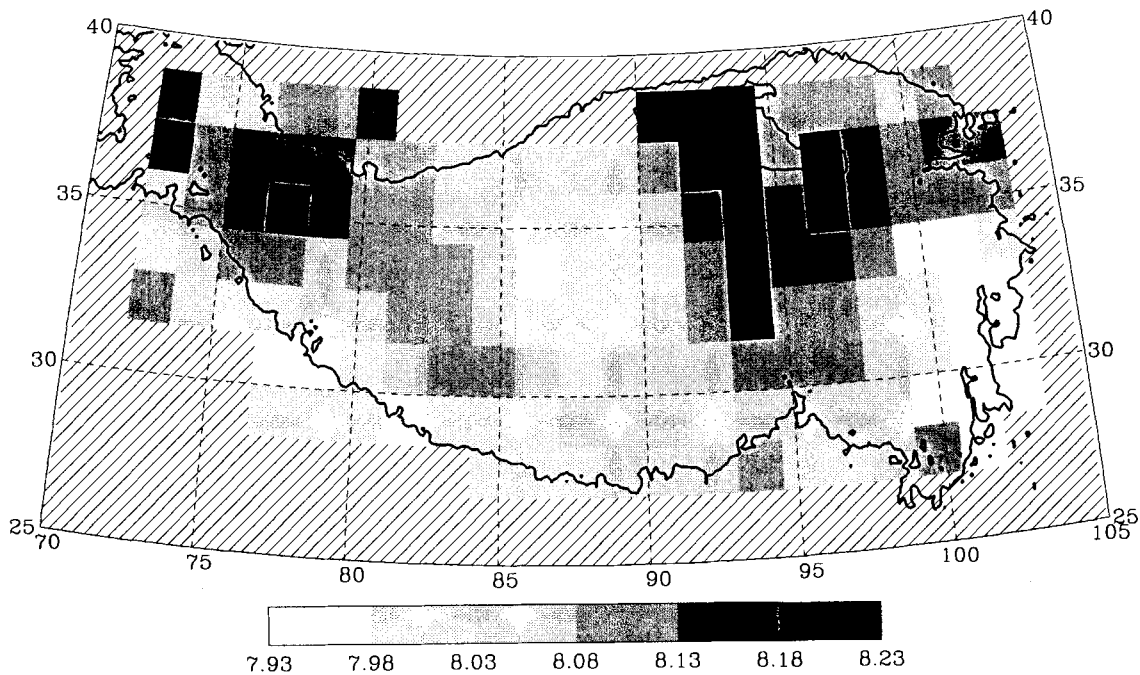
Figure 8. 2-D P-velocity image obtained without correcting for the mantle-velocity gradient.

for both P_n tomographies (e.g. Hearn *et al.* 1991) and for the P_n studies in and around Tibet (Chen & Molnar 1981; Barazangi & Ni 1982; Ni & Barazangi 1983). Zhao & Helmberger (1991) found that the locations by ISC lead to an overestimation of about 1.5 per cent for P_n velocity in Tibet. Holt & Wallace (1990) also found that ISC locations of Tibetan events were systematically too deep, leading to higher velocity estimates. To test the effects of not conducting event relocation, we conducted the back-

projection inversion using the parameters reported by ISC bulletins, with corrections of a'_i, b'_j calculated using model TIP, and without the corrections of mantle-velocity gradient. The resulting P-velocity image is plotted in Fig. 10, where the average velocity is 8.28 ± 0.19 km s^{-1}, which is similar to 8.42 km s^{-1} suggested by Barazangi & Ni (1982) and by Ni & Barazangi (1983). The main pattern of slower velocities in north central Tibet is no longer clear in Fig. 10, and many of the faster velocities in the flanks of Tibet in
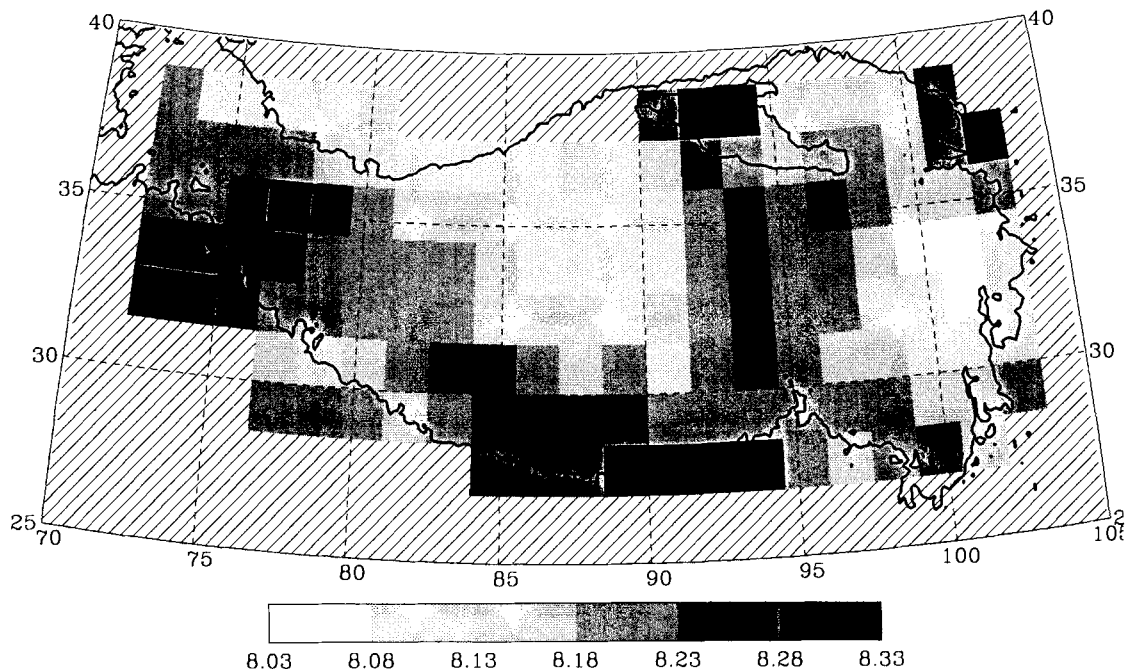

Figure 9. 2-D P-velocity image obtained with no corrections to the mantle-velocity gradient, nor to the regionally varying vertical traveltimes from source/station to Moho.
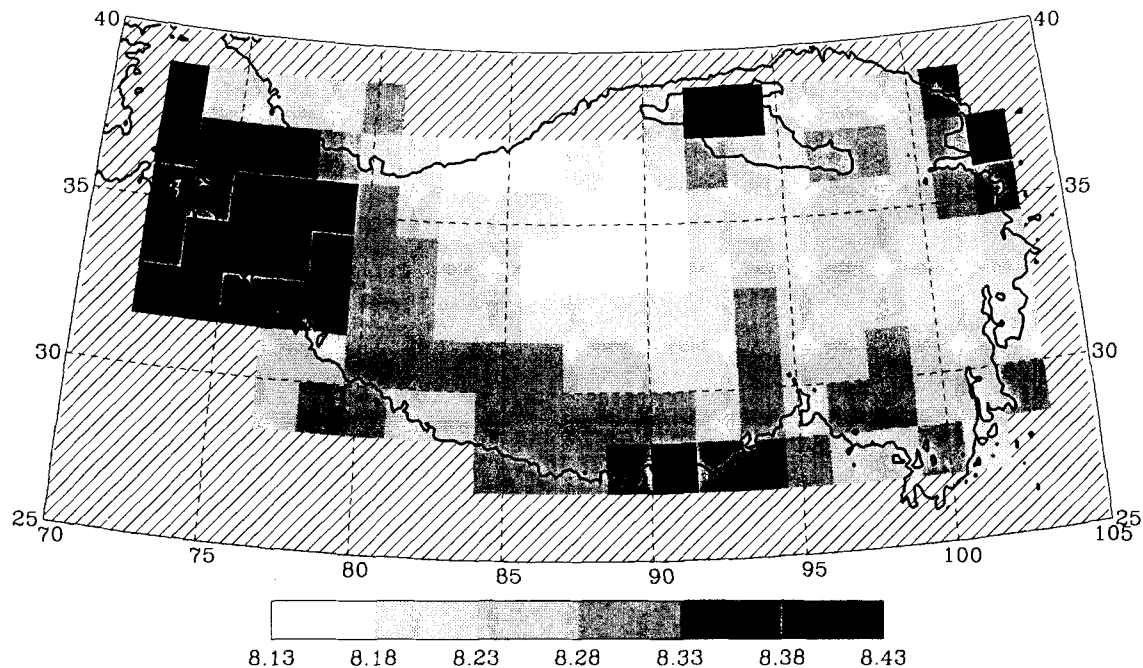
Figure 10. 2-D P-velocity image obtained by using all parameters, including P_n-arrival time picks and the event-origin times/locations, from the ISC bulletins.

Figs 4, 8 and 9 are now outside Tibet. Fig. 10 gives one a misconception that nearly all of Tibet forms a large low-velocity region. This test, therefore, indicates that it is extremely important to relocate the events in a P_n tomography study, at least for an area like Tibet.

Errors in the crustal-thickness estimates

When estimating crustal thicknesses, we have ignored the probable effects on the remnant residuals, systematically caused in each of the 28 subregions, by (1) origin-time errors, (2) erroneous P_n arrival readings, and (3) the deviation of the real Moho interface from the gridded, smoothly varying surface. Ignoring all of these effects may lead to erroneous results. However, that high-level structural variations have been known to exist in Tibet (e.g. Hirn & Sapin 1984) suggests that these effects should be, to the first order, negligible, and that the crustal thickness thus obtained should serve as first-order approximations. We also think that the crustal thicknesses inferred for subregions with less than 10 arrivals (Table 3) may not be reliable, since the corresponding inverse matrix is near singular.

DISCUSSION AND CONCLUSIONS

353 P_n traveltimes from 44 Tibetan earthquakes and at 46 seismic stations have been collected to study lateral variations in compressional velocity in the uppermost mantle underneath the Tibetan Plateau. The inverse method and procedures of this study differ from those in previous P_n tomographies in that in the current study we applied, to the traveltime measurements, corrections to several important biases, such as those caused by (1) event mislocation by ISC, (2) mantle-velocity gradient and (3) regional variations in crustal thicknesses.

We used a back-projection algorithm to obtain a 2-D

P-velocity image for the uppermost mantle. We also inverted for, to the first order, the crustal thicknesses in 28 subregions in and around Tibet.

The main results of the inversion are: (1) the average P-velocity value for the uppermost mantle in Tibet is $7.93 \pm 0.17 \, \text{km s}^{-1}$, (2) the average P-velocity gradient in the upper 150 km of the mantle is $3.1 \times 10^{-3} \, \text{s}^{-1}$; (3) the 2-D P-velocity image of the region includes a low-velocity zone in north central Tibet, and two high-velocity zones in the western and eastern flanks of Tibet; (4) the crustal thickness is greater than 70 km inside Tibet, it decreases toward the boundaries of the Plateau.

Comparison of our 2-D P-velocity image and estimates of the crustal thicknesses with those obtained in previous localized studies shows general agreements within the uncertainties. A few exceptions can be explained by various complications in P_n propagation, such as the effects of mantle-velocity gradient, which has not been taken in to account in most previous studies.

The spatial resolution of our P-velocity image is generally within 10°, and often within 6° where the ray coverage is dense. The random error in the image is estimated to be generally within about $0.02 \, \text{km s}^{-1}$ for locations inside Tibet. However, systematic, 'modelization' errors may be greater.

Another important finding of this study is that event relocation (correction to bias (1) mentioned earlier) plays a very important role in reliably retrieving the detailed lateral variations in 2-D P-velocity image. Corrections to biases (2) and (3) mentioned earlier, on the other hand, seem to have a greater effect on the average (DC level) of the velocity image; the average P velocity is overestimated without these corrections.

The low-velocity region in north central Tibet found in this study coincides with the locations of low-S–P traveltime residuals found in localized studies by Molnar & Chen

(1984), Pettersen & Doornbos (1987) and Molnar (1990). It also overlaps with the area where Neogene or younger volcanic rocks have been found (Burke *et al.* 1974; Kidd 1975; Deng 1978; Sengor & Kidd 1979; Molnar *et al.* 1987). These support the hypothesis by Molnar (1988, 1990) that a convective upwelling may be occuring in north central Tibet, and downwelling occuring in surrounding regions.

ACKNOWLEDGMENTS

REFERENCES

Barazangi, M. & Ni, J., 1982. Velocities and propagation characteristics of *Pn* and *Sn* beneath the Himalayan arc and Tibetan plateau: possible evidence for underthrusting of Indian continental lithosphere beneath Tibet, *Geology*, **10**, 179–185.

Beloussov, V. V., Belyaevsky, N. A., Borisov, A. A., Volvovsky, B. S., Volkovsky, I. S., Resvoy, D. P., Tal-Virsky, B. B., Khamrabaev, I. Kh., Kaila, K. L., Narain, H., Marussi, A. & Finetti, J., 1980. Structure of the lithosphere along the deep seismic sounding profile: Tien Shan–Pamirs–Karakoram–Himalayas, *Tectonophysics*, **70**, 193–221.

Bourjot, L. & Romanowicz, B., 1992. Crust and upper mantle tomography in Tibet using surface waves, *Geophys. Res. Lett.*, **19**, 881–884.

Burke, K. C., Dewey, J. F. & Kidd, W. S. F., 1974. The Tibetan Plateau: its significance for tectonics and petrology, *Geol. Soc. Am. Abstr. Prog.*, **6**, 1027–1028.

Chen, Wang-Ping & Molnar, P., 1981. Constraints on the seismic wave velocity structure beneath the Tibetan Plateau and their tectonic implications, *J. geophys. Res.*, **86**, 5937–5962.

Deng, W. M., 1978. Preliminary study on the petrology and petrochemistry of the Quaternary volcanic rocks, northern Tibetan Autonomous Regions, *Acta Geol. Sin.*, **2**, 148–162 (in Chinese, English abstract).

Feng, R., 1985. Crustal thickness and densities in the upper mantle beneath China—the results of three dimensional gravity inversion, *Acta Seism. Sin.*, **7**, 143–157 (in Chinese, English abstract and figure captions).

Feng, R., Zhu, J. S., Ding, Y. Y., Chen, G. Y., He, Z. Q., Yang, S. B., Zhou, H. N. & Sun, K. Z., 1981. Crustal structure in China from surface waves, *Acta Seism. Sin.*, **3**, 335–350 (in Chinese, English abstract and figure captions).

Hearn, T. Beghoul, N. & Barazangi, M., 1991. Tomography of the Western United States from regional arrival times, *J. geophys. Res.*, **96**, 16 369–16 381.

Helmberger, D. V., 1973. Numerical seismograms of long-period body waves from seventeen to forty degrees, *Bull. seism. Soc. Am.*, **63**, 633–646.

Hirn, A., Jobert, G., Wittlinger, G., Xu, Z. X. & Gao, E. Y., 1984a. Main features of the upper lithopshere in the unit between the high Himalayas and the Yarlung Zangbo Jiang suture, *Ann. Geophys.*, **2**, 113–118.

Hirn, A., Leipine, J.-C., Jobert, G., Sapin, M., Wittlinger, G., Xu, Z. X., Gao, E. Y., Wang, X. J., Teng, J. W., Xiong, S. B., Pandey, M. R. & Tater, J. M., 1984b. Crustal structure and variability of the Himalayan border of Tibet, *Nature*, **307**, 23–25.

Hirn, A., Nercessian, A., Sapin, M., Jobert, G., Xu, Z. X., Gao, E. Y., Lu, G. Y. & Teng, J. W., 1984c. Lhasa block and bordering sutures—a continuation of a 500-km Moho traverse through Tibet, *Nature*, **307**, 25–27.

Hirn, A. & Sapin, M., 1984. The Himalayan zone of crustal interaction: suggestions form explosion seismology, *Ann. Geophys.*, **2**, 123–130.

Holt, W. E. & Wallace, T. C., 1990. Crustal thickness and upper mantle velocities in the Tibetan Plateau regions from the inversion of regional P_{nl} waveforms: evidence for a thick upper mantle lid beneath southern Tibet, *J. geophys. Res.*, **95**, 12 499–12 525.

Hu, H. X., Lu, H. X., Wang, C. Y., He, Z. Q., Zhu, L. B., Yan, Q. Z., Fan, Y. X., Zhang, G. Q. & Deng, Y. E., 1986. Explosion investigation of the crustal structure in western Yunnan Province, *Acta Geophys. Sin.*, **29**, 133–144 (in Chinese, English abstract).

Humphreys, E. & Clayton, R. W., 1988. Adaptation of back projection tomography to seismic travel time problems, *J. geophys. Res.*, **93**, 1073–1086.

Institute of Geophysics, Chinese Academy of Sciences, 1981. Explosion seismic study for velocity distribution and structure of the crust and upper mantle for Damxung to Yadong of Xizang (Tibet) Plateau, *Acta Geophys. Sin.*, **24**, 155–170 (in Chinese, English abstract).

Jia, S. J. & Chao, X. F., 1981. *P* wave travel times and upper mantle velocity structure beneath Qinghai-Xizang Plateau, *N. West Seism. J.* **3**, 27–34.

Kaila, K. L., 1981. Structure and seismotectonics of the Himalaya—Pamir Hindu Kush region and the Indian plate boundary, in *Zagros—Hindu Kush—Himalaya Geodynamic Evolution*, pp. 272–293, eds Gupta, H. K. & Delany, F. M., Am. geophys. Un., Washington DC.

Kaila, K. L., Reddy, P. R. & Narin, H., 1968. Crustal structure in the Himalayan Foot Hills area of north India, from *P* wave data of shallow earthquakes, *Bull. seism. Soc. Am.*, **58**, 597–612.

Kan, R. J. & Lin, Z. Y., 1988. A preliminary study on the crustal and upper mantle structure in Yunnan, *Earthq. Res. China*, **2**, 183–202.

Kidd, W. S. F., 1975. Widespread late neogene and quaternary calc-alkaline volcanism on the Tibetan Plateau, *EOS, Trans. Am. geophys. Un.*, **56**, 453.

Molnar, P., 1988. A review of geophysical constraints on the deep structure of the Tibetan Plateau, the Himalaya and the Karakoram, and their tectonic implications, *Phil. Trans. R. Soc. Lond.*, A, **326**, 33–88.

Molnar, P., 1990. *S*-wave residuals from earthquakes in the Tibetan region and lateral variations in the upper mantle, *Earth planet. Sci. Lett.*, **101**, 68–77.

Molnar, P. & Chen, W. P., 1984. *S–P* wave travel time residuals and lateral inhomogeneity in the mantle beneath Tibet and the Himalaya, *J. geophys. Res.*, **89**, 6911–6917.

Molnar, P., Burchfield, B. C., Zhao, Z. Y., Liang, K. Y., Wang, S. J. & Hung, M. M., 1987. Geologic evolution of Northern Tibet: results of an expedition to Ulugh Muztagh, *Science*, **235**, 299–305.

Nelson, K. D., Brown, L. D., Hauk, M. L. & Kuo, J. T., 1993. Imaging the India–Asia decollement beneath sourthern Tibet; Project INDEPTH deep seismic profiling results. *EOS, Trans. Am. geophys. Un. Supplement, 1993 Spring Meeting*, **302**, Am. geophys. Un., Washington, DC.

Ni, J. & Barazangi, M., 1983. High-frequency seismic-wave propagation beneath the Indian Shield, Himalayan arc, Tibetan Plateau and surrounding regions: high-uppermost mantle velocities and efficient S_n propagation beneath Tibet, *Geophys. J. R. astr. Soc.*, **72**, 665–681.

Pettersen, O. & Doornbos, D. J., 1987. A comparison of source analysis methods as applied to earthquakes in Tibet, *Phys. Earth planet. Inter.*, **47**, 125–136.

Sapin, M., Wang, X. J., Hirn, A. & Xu, Z. X., 1985. A seismic sounding in the crust of the Lhasa block, Tibet, *Ann. Geophys.*, **3**, 637–646.

Sengor, A. M. C. & Kidd, W. S. F., 1979. Post-collisional tectonics of the Turkish-Iranian Plateau and a comparison with Tibet, *Tectonophysics*, **55**, 361–376.

Song, Z. H., An, C. Q., Wang, C. Y., Zhang, L. J. & Qiu, Z. R., 1985. The P wave velocity of upper mantle beneath Qinghai-Tibet Plateau and North–South seismic zone, *Acta Geophys. Sin.*, **28**, (Supplement I), 148–160 (in Chinese, English abstract).

Tarantola, A., 1987. *Inverse problem theory*, Elsevier, New York.

Teng, J. W., Xiong, S. P., Sun, K. Z., Yin, Z. X., Yao, H., Chen, L. F., Mu, T., Lai, M. H., Wu, M. C., Su, D. Y., Wang, S. Z., Huang, W. J., Ou, R. S., Hao, W. C., Shao, A. M., Gao, E. Y., Wang, M. L., Lin, Z. Y. & Qu, K. X., 1981.Explosion seismological study for velocity distribution and structure of the crust and upper mantle from Damxung to Yadong of the Xizang Plateau, *Acta Geophys. Sin.*, **24**, 155–170 (in Chinese, English abstract). Also in *Geological and Ecological Studies of Qinghai—Xiang Plateau*, Science Press, Beijing.

Teng, J. W., Sun, K. Z., Xiong, S. B., Yin, Z. X., Yao, H. & Chen, L. F., 1983a. Deep seismic reflection waves and structure of the crust from Dangxung to Yadong on the Xizang Plateau (Tibet), *Phys. Earth planet. Inter.*, **31**, 293–306.

Teng, J. W., Xiong, S. B., Yin, Z. X., Xu, Z. X., Wang, X. J., Lu, D. Y., Jobert, G. & Hirn, A., 1983b. Structure of the crust and upper mantle pattern and velocity distributional characteristics at northern region of the Himalayan mountains, *Acta Geophys. Sin.*, **26**, 525–540 (in Chinese, English abstract).

Teng, J. W., Xiong, S. B., Yin, Z. X., Wang, X. J. & Lu, D. Y., 1985a. Structure of the crust and upper mantle pattern and velocity distributional characteristics in the northern Himalayan mountain region, *J. Phys. Earth*, **33**, 157–171.

Teng, J. W., Yin, Z. X. & Xiong, S. B., 1985b. Crustal structure and velocity distribution beneath the Serlin Co–Peng Co—Naqu—Suo county region in the northern Xizang (Tibet) Plateau, *Acta Geophys. Sin.*, **28**, (Supplement I) 28–42 (in Chinese, English abstract).

Verma, G. S., 1974. Structure of the foot-hills of the Himalayas, *Pure appl. Geophys.*, **112**, 18–26.

Xie, J. & Mitchell, B. J., 1990. A back-projection method for imaging large-scale lateral variations of Lg coda Q with application to continental Africa, *Geophys. J. Int.*, **100**, 161–181.

Xiong, S. B., Teng, J. W. & Yin, Z. X., 1985. The thickness of the crust and undulation of discontinuity in Xizang (Tibet) Plateau, *Acta Geophys. Sin.*, **28**, (Supplement I), 16–27 (in Chinese, English abstract).

Xiong, S. B., Teng, J. W., Yin, Z. X., Lai, M. H. & Huang, Y. P., 1986. Explosion seismological study of the structure of the crust and upper mantle at southern part of the Panxi tectonic belt, *Acta Geophys. Sin.*, **29**, 235–244 (in Chinese, English abstract).

Yin, X. H., Liu, Z. P., Wu, J. X., Wang, C. H. & Liu, T. S., 1988. The features of Bouguer gravity field and structures of crust—upper mantle in the transition zone on the eastern border of Qinghai–Xizang–Mongolian Plateau, *Seismology and Geology*, **10**, 143–150 (in Chinese, English abstract and figure captions).

Zhao, D., Hasegawa, A. & Hirouchi, S., 1992. Tomographic imaging of P and S wave velocity structure beneath northeastern Japan, *J. geophys. Res.*, **97**, 19 909–19 928.

Zhao, L. S., 1993. Lateral variations in Pn velocities beneath Basin and Range province, *J. geophys. Res.*, in press.

Zhao, L. S. & Helmberger, D. V., 1991. Geophysical implications from relocations of Tibetan earthquakes: hot lithosphere, *Geophys. Res. lett.*, **18**, 2205–2208.

Zhao, L. S. & Helmberger, D. V., 1993. Source retrieval from broadband regional seismograms; Hindu Kush region, *Phys. Earth planet. Inter.*, **78**, 69–95

Zhao, Z. & Zhang, R. S., 1987. Primary study of crustal and upper mantle velocity structure of Sichuan Province, *Acta Seism. Sin.*, **9**, 154–166 (in Chinese, Englsh abstract and figure captions).

Zhao, L. S., Helmberger, D. V. & Harkrider, D. G., 1991. Shear-velocity structure of the crust and upper mantle beneath Tibetan and southeastern China, *Geophys. J. Int.*, **105**, 713–730.

Zhu, P. D., Li, Y. M., Zhang, L. M., Shu, P. Y. & Liang, S. H., 1986. On the study of the crust and upper mantle structure beneath the seismic telemetry network in south Sichuan and north Yunnan Provinces, *Acta Geophys. Sin.*, **29**, 245–254 (in Chinese, English abstract).

APPENDIX: DERIVATION OF EQUATIONS (5)

We assume that the mantle velocity is given by eq. (4), i.e.

$$v(z) = v_0(1 + cz), \tag{A1}$$

where we assumed $z_0 = 0$ for simplicity. For head waves (such as P_n) turning at a depth, h, the ray parameter is $1/v(h)$, and the traveltime $T(h)$ is given by:

$$T(h) = \frac{X}{v(h)} + 2\int_0^h \left(\frac{1}{v(z)^2} - \frac{1}{v(h)^2}\right)^{1/2} dz$$

$$= \frac{1}{v_0(1+ch)}\left[X - \frac{2}{c}[(1+ch)^2 - 1]^{1/2}\right.$$

$$\left. + \frac{2(1+ch)}{c} \ln\{1 + ch + [(1+ch)^2 - 1]^{1/2}\}\right], \tag{A2}$$

where X is the horizontal distance travelled in the mantle. The head-wave traveltime over X should satisfy $dT(h)/dh = 0$, we have:

$$X = \frac{2}{c}[(1+ch)^2 - 1]^{1/2}, \tag{A3}$$

and the head-wave traveltime over X is;

$$T = \frac{2}{v_0 c} \ln\{1 + ch + [(1+ch)^2 - 1]^{1/2}\}. \tag{A4}$$

From definition, the observed head-wave velocity is

$v_{obs} = X/T$. From (A3) and (A4) we have:

$$v_{obs} \approx v_0 \frac{\sqrt{2ch}\,(1 + ch/4)}{\ln(1 + ch + \sqrt{2ch}\,(1 + ch/4))}$$

$$\approx v_0 \frac{\sqrt{2ch}\,(1 + ch/4)}{\sqrt{2ch}\,(1 - ch/12)}$$

$$\approx v_0\left(1 + \frac{ch}{3}\right), \tag{A5}$$

if $ch \ll 1$. For $ch \ll 1$, X can be approximated by

$$X \approx \sqrt{8h/c}, \quad \text{or} \quad h \approx cX^2/8. \tag{A6}$$

Substituting (A6) into (A5), we have eq. (5) in the text.

$$v_{obs} \approx v_0(1 + c^2X^2/24).$$